Journal of Nuclear Materials 381 (2008) 171–176

Contents lists available at ScienceDirect

Journal of Nuclear Materials

journal homepage: www.elsevier.com/locate/jnucmat

Microstructural scale strain localisation in nuclear graphite

M.R. Joyce, T.J. Marrow *

Materials Performance Centre, University of Manchester, Manchester, UK

ARTICLE INFO

PACS:
62.20.Mk

ABSTRACT

The surface strain fields evolved during disc compression tests on virgin IM1-24 were obtained via electronic speckle pattern interferometry (ESPI). A methodology for characterising strain localisation on a microstructural scale is presented, which provides a quantitative description of the damage localisation and failure processes.

1. Introduction

A full understanding of the effects of microstructural degradation on the fracture of nuclear graphite requires models for the nucleation and coalescence of damage under the influence of different strain states, including strain gradients at stress concentrations such as notches. A preliminary step towards this is the characterisation of strain localisation, caused by microstructural features, under applied loading. In situ strain mapping can provide the necessary observations of this process, albeit only on the sample surface. The aim of this work is to establish a methodology for determining the statistical distribution of microstructural strains in virgin Gilsocarbon (IM1-24), and furthermore to provide an insight into the failure process. It is known that fracture in this material involves the propagation of micro-cracks [1], and it is anticipated that strain localisation is a precursor to crack development.

2. Experimental methodology

Disc compression tests were performed using specimens of IM1-24 graphite with a radius and thickness of 10 mm. Reliable measurements of tensile fracture strength in the disc compression test are only possible if the sample fails in tension at its centre [2]. In practice this requires that the loading be distributed along a prescribed length of the disc periphery [3], which may be achieved using curved anvils. Alternatively, two diametrically opposed flats can be machined into the samples, as suggested by Wang et al. [4]. Such an approach eases both sample preparation and experimental set-up, and hence flattened regions of 5 mm width were machined into the samples employed in this work. The load, P, was applied in displacement control using an Instron 5802 electro-mechanical frame at a rate of 0.05 mm min^{-1} until sample failure occurred at the peak load, P_{max}. Full field displacement measurements were made using the Dantec Dynamics Q-300 ESPI system. This comprises a single CCD camera (576 × 768 pixels) and both in-plane and out-of-plane laser interferometers, thereby permitting 3D deformations to be obtained. To maximise the number of pixels used, the optical magnification was such that the sample filled almost the full width of the imaged region. In each test the sample was loaded progressively from a small pre-load (<100 N) without interruption until the sample failed. Deformation measurements were made at 100 N increments using the 'four bucket' method, hence four interferograms at incremental optical phase shifts of $\pi/2$ were recorded by each of the 3 interferometers. This procedure took ~2.5 s to complete, but due to the slow cross head displacement rate the sample deformation during this time was considered negligible. The typical duration of each test was 1200 s.

3. Analysis methodology

The interferograms were analysed and phase maps un-wrapped using the '4-bucket' technique implemented in the 'Istra' software package supplied by Dantec Dynamics. This permitted deformation fields in each of three interferometer axes to be produced at 100 N load increments. Examples of the horizontal phase and deformation maps are shown in Fig. 1. Whilst deformation maps were obtained in three dimensions and across the whole of the sample surface, detailed analysis was restricted to the central region of the in-plane deformations as indicated in Fig. 1. This restriction was implemented since the deformations at the sample edges, particularly near the loading platens are likely to be spurious. The resulting maps cover an area of 100 mm^2 and contain ~13 000 pixels, each providing a discrete deformation value.

The measured strain fields comprise the underlying strain state inherent to the sample geometry in conjunction with perturbations caused by microstructural inhomogeneities. In order to study and

* Corresponding author. Tel.: +44 (0) 161 306 4915; fax: +44 (0) 161 306 3586.
E-mail address: james.marrow@manchester.ac.uk (T.J. Marrow).

0022-3115/$ - see front matter © 2008 Published by Elsevier B.V.
doi:10.1016/j.jnucmat.2008.07.013

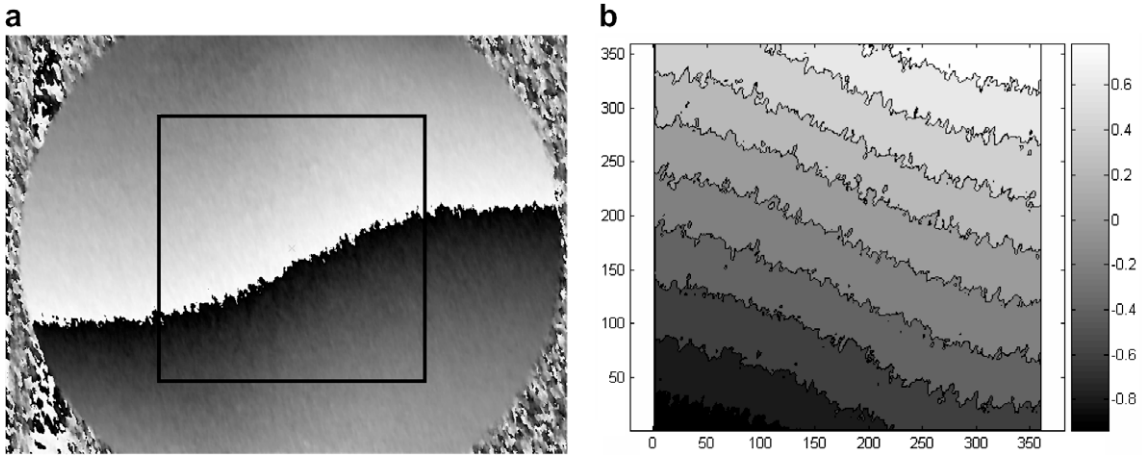

Fig. 1. (a) Horizontal ESPI phase map showing the region to which subsequent analysis is restricted; (b) example of incremental horizontal deformation between an image pair (deformation scale bar in microns, horizontal and vertical axes in pixels).

characterise the later, the former must be removed. In a more simple testing geometry (i.e. uniaxial tension) the strain state might be assumed uniform, and hence the microstructural strain component extracted simply by subtracting the mean strain value. However, since the strain state in the disc compression geometry is both biaxial and non-uniform a more thorough treatment is appropriate. This was done by correlating the measured fields with those obtained from an elastic finite element model. Whilst analytical stress solutions are available for the disc compression sample and have been applied by other authors [5,6], they cannot be used in this case due to the flattened disc samples adopted in this study. Furthermore, since the elastic constants were unknown the model deformation field was fitted to the measured solutions using an optimisation approach. Estimations of the Young's modulus and Poisson's ratio were therefore obtained.

4. Finite element correlation and global elastic properties

The correlation and optimisation procedure could equally be carried out in terms of deformation or strain. However a degree of noise is present in the measured deformation fields, the magnitude of which will be greatly increased by the differentiation required to produce strain fields. In turn this will affect how well the finite element solutions correspond to the experimental results. Therefore the correlation was performed in terms of deformation; however this approach does require sample rigid body movement to be accounted for. In practise, this is not a great limitation since the ESPI deformation measurements are not absolute, but are made relative to the disc centre, which was chosen as the origin during the fringe un-wrapping procedure. Whilst in-plane translation is therefore zero, the rotation around the axis normal to the sample surface must be addressed. This was achieved by assuming that the neutral axis for the horizontal deformation field should be vertical, and the converse for the corresponding vertical deformation field. Fig. 2(a) and (b) show examples of the measured horizontal and vertical deformation fields. Clearly the observed neutral axes are not aligned as anticipated. Fig. 2(c) and (d) show the same fields after a uniform rotational transformation has been applied to bring the neutral axes into the correct orientation. This procedure was implemented systematically for each pair of in-plane fields throughout the duration of each test. Whilst the transformation applied was typically less than 0.5, failure to correct for it would lead to a systematic error in the results since sample rotation was found to generally increase with load.

The finite element model was formulated in three dimensions using geometric symmetric planes and meshed with 20-noded brick elements. A linear elastic material model was employed and the model solved using the Abaqus 6.5 general purpose finite element code. Nodal deformations were obtained from the region of the free surface corresponding that observed in the experimental studies. Solutions were obtained at fixed known values of applied load and Young's modulus, across a range of Poisson's ratios from 0.05 to 0.49 in 0.01 increments. These data essentially provide a look up table for the subsequent optimisation procedure. The mesh design and an example solution for the horizontal deformation field are shown in Fig. 3.

To avoid excessive computation the FE fields were of significantly lower spatial resolution than the ESPI measurements, hence before the optimisation process could begin the FE solutions were interpolated onto the grid defined by the experimental observations using the original element shape functions. To start the optimisation, the measured deformation fields were overlaid with the interpolated FE fields obtained using arbitrary values of Young's modulus and Poisson's ratio. The error, Err, over n measurement points, between the two pairs of fields or the penalty function was given by Eq. (1)

$$\mathrm{Err} = \frac{\sum_{i=1}^{n}\left[\left(\frac{\delta_{H,\mathrm{exp}}-\delta_{H,\mathrm{FE}}}{\delta_{H,\mathrm{FE}}}\right)^2+\left(\frac{\delta_{V,\mathrm{exp}}-\delta_{V,\mathrm{FE}}}{\delta_{V,\mathrm{FE}}}\right)^2\right]}{n} \tag{1}$$

where the subscripts 'FE' and 'exp' refer to the finite element and experimentally derived deformation (δ) values in the horizontal (H) and vertical (V) directions at a given pixel. The best fit elastic constants were obtained by employing a constrained minimisation approach to vary Young's modulus and Poisson's ratio to obtain the best fit between the measured and FE derived deformation fields. This procedure was repeated for each pair of measured deformation fields throughout the test; hence the evolution of these constants with applied load was derived and is shown in Fig. 4.

No attempt was made to fit the FE solution to the deformation fields obtained below an applied load of 1000 N. Spurious deformations due to sample settling prevented meaningful results being obtained. Furthermore, since in the ESPI analysis the total deformations are accumulated from all the incremental deformations between pairs of images, any spurious deformations obtained at low loads would have a detrimental influence on the results throughout the test. Above 1000 N the Young's modulus results are reasonably consistent and have an average value of 8.47 ± 0.85 GPa, which compares well with the expected value

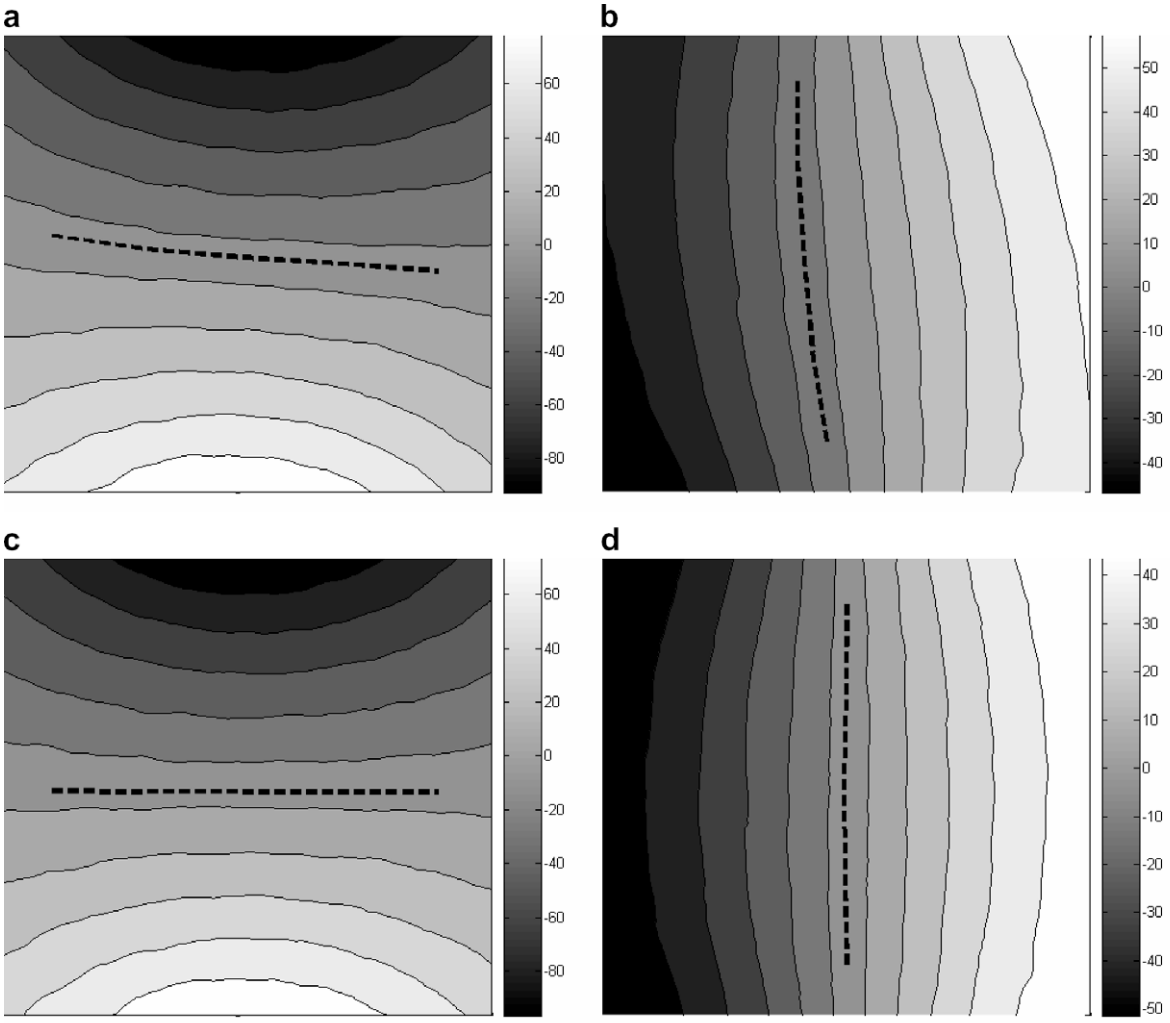

Fig. 2. Example in-plane deformations. (a and b) measured deformation in the horizontal and vertical directions respectively. (c and d) deformations corrected for rotation around the axis normal to the sample surface. Neutral axes indicated by dashed lines, scale bar in microns.

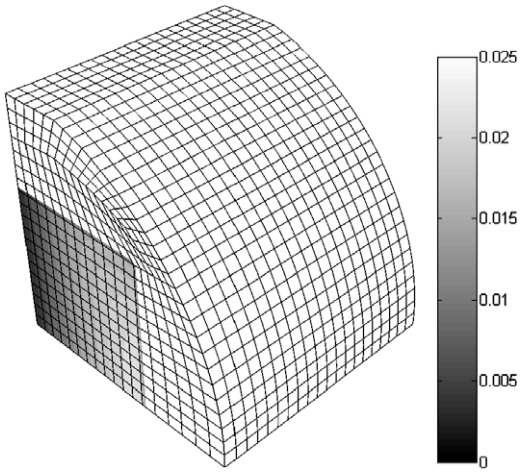

Fig. 3. Finite element model showing element density and an example horizontal deformation field solution. Scale bar in microns.

for Gilsocarbon [7]. Whilst three tests shown in Fig. 4 returned a constant modulus value, some non-linearity with increasing load was indicated in the other two although not to the degree reported by Taylor et al. [7].

The Poisson's ratio appears constant at low loads, before showing a generally rising trend towards sample failure. Strain dependence of Poisson's ratio has not been reported previously. However, the average value of 0.22 ± 0.03 is consistent with literature values for this graphite grade [7].

That the recovered elastic constants are in agreement with the expected values, gives confidence that an appropriate baseline has been fitted to the data. It therefore appears appropriate to use this methodology for removing the intrinsic effect of sample geometry, hence permitting investigation of the microstructural perturbations.

5. Microstructural strain visualisation

At each load increment of each tested sample, the fitted global deformation fields were subtracted from the measured fields thereby leaving the perturbations associated with microstructural inhomogeneities. However, in order to analyse these features further, strain fields rather than deformation fields are required. Strains could be obtained by differentiating the deformation fields directly, using a finite difference approach over a linear range of pixels. However, in practice this approach tends to smear the features in the differentiation direction. Instead bi-linear piecewise functions were fitted to 5×5 pixel regions of the disc surface.

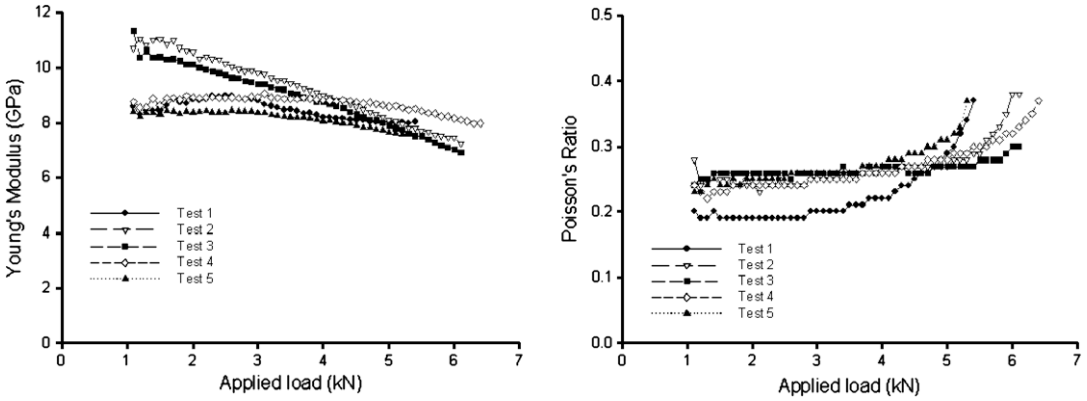

Fig. 4. Evolution of apparent global Young's modulus and Poisson's ratio obtained from disc compression test.

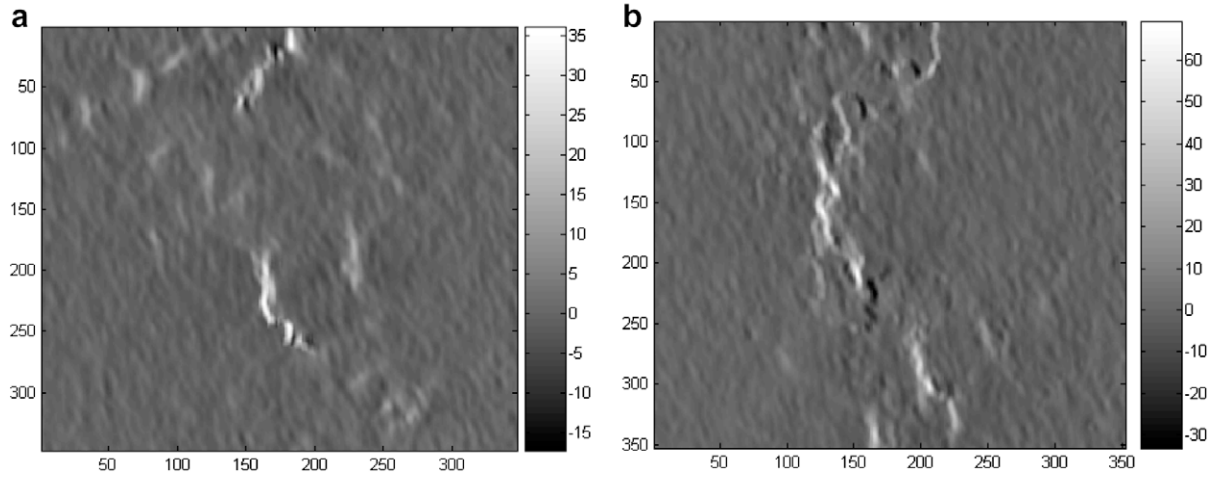

Fig. 5. Horizontal strain fields obtained from two samples, by fitting bi-linear functions to local disc regions. Scale bar in millistrain. The horizontal and vertical axes are in pixels (1 pixel = 28 μm).

This dimension, corresponding to an area of 0.02 mm^2, was selected to provide a compromise between resolving small features and rejecting excessive noise. The surface strains could then be obtained from the gradients of these closed form functions. However, it is important to note that these 'strains' are not directly indicative of those present within the microstructure. Rather they are analogous to the output of a 0.02 mm^2 strain gauge located on that point of the sample surface. Nonetheless, microstructurally-induced strain perturbations should be detectable using this method. As applied the technique has a pixel resolution of ~28 μm, albeit effectively smoothed over a length of ~140 μm. This is significantly smaller than the typical pore dimensions of up to several hundred μm and filler particle size of more than 500 μm.

In well aligned disc compression tests with appropriately distributed loading, the mode of failure is by vertical splitting [2], due to tensile stresses evolved at the disc centre. This mode of failure was observed in all the tests. Hence it is assumed that the cracking and strain localisation that is a precursor to failure will be most evident in the horizontal tensile direction. Therefore, the strain localisation has only been fully characterised in the horizontal direction. Fig. 5 shows examples of the horizontal microstructural strain fields, immediately prior to failure, obtained by the method described from the central region of a disc compression sample.

That microstructure strongly influences strain formation is clearly evident, since the strain maps in Fig. 5 show that significant points of strain localisation are produced on the surface of the disc compression samples. It is hypothesised that characterising the distribution and behaviour of the high strain regions will provide a valuable insight into the deformation and fracture behaviour of this material.

6. Microstructural strain distribution and evolution

The microstructural strain images shown in Fig. 5 show the error obtained by subtracting the measured strain from that predicted by the FE model. These results may be biased, since the inherent strain is greater at the disc centre and hence the magnitude of the microstructural strain is likely to be greater in these regions. To characterise the effect of microstructure on the local strain, it is more correct to consider the behaviour of the ratio between the measured and predicted strains. The frequency distribution of this parameter, termed 'strain ratio', is shown in Fig. 6 for the horizontal tensile fields evolved at loads of 25% and 95% of P_{max}.

If strain localisation is negligible, the distribution should appear as a delta function, i.e. a single line centered at value of one. However, as shown in Fig. 6(a), the microstructure has a significant effect and the distribution adopts an approximately Gaussian shape.

However, as the applied load increases, the distribution shape changes significantly, as shown in Fig. 6(b); the main peak shift towards lower strains; a marked high strain 'shoulder' develops and immediately prior to failure very high strains are indicated. These

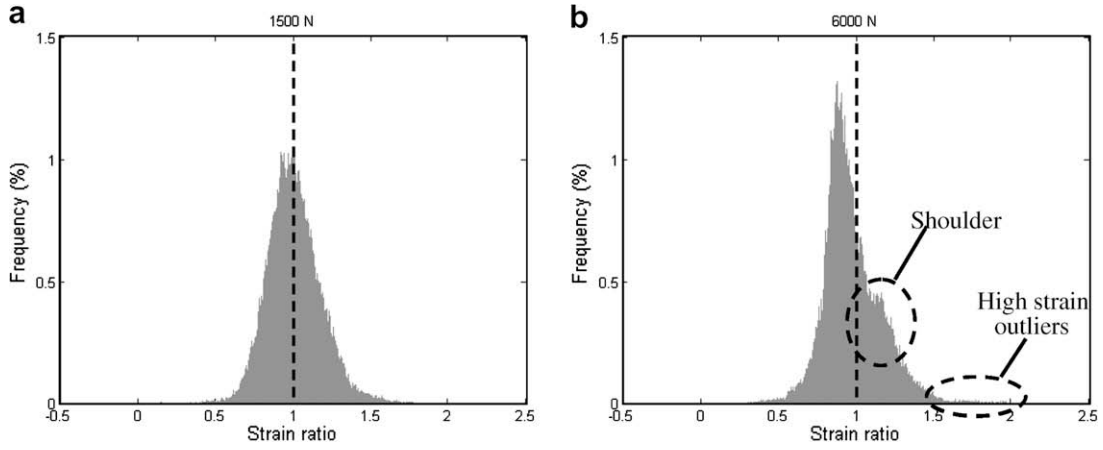

Fig. 6. Microstructural strain ratio distributions at; (a) 25% and (b) 95% of P_{max}.

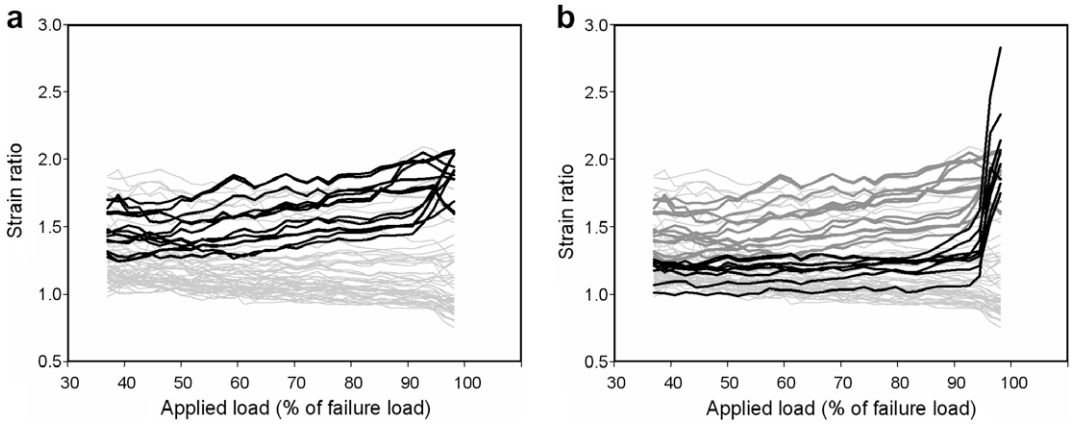

Fig. 7. Evolution of maximum strain ratio within each domain with increasing load; (a) domains not involved with failure; (b) including failure domains.

changes are consistent with the severe strain localisation as shown in Fig. 5.

The strain ratio distribution alone cannot be used to fully characterise microstructural strain localisation, since it does not give any insight into spatial characteristics of the strain localisation process. Inspection of the tensile strain field with increasing load, e.g. Fig. 5, shows that high strains appear to be localised at a finite number of well defined points rather than randomly distributed. The degree of strain accumulation during loading may therefore be characterised for these individual regions of high strain. The strain ratio fields were divided into domains of 2 mm^2, the maximum value within each domain was noted and the evolution of strain ratio within each domain is plotted for one sample in Fig. 7.

The light grey lines in Fig. 7(a) show that the strain ratio in the majority of domains remained constant throughout the test. Although several of these exhibit consistently high strain ratios they do not appear to develop or contribute to the failure process. In contrast a generally rising strain ratio trend was observed in ~15% of the domains (shown in black in Fig. 7(a)). These were spatially well distributed and typically begin to rise above ~50% of P_{max}. Finally, as shown in Fig. 7(b), failure is associated with relatively few domains. In this example 3 domains near the disc centre show a marked rise at ~85% of P_{max}, followed by a more dramatic rise at ~95% of P_{max}. This latter rise is matched by corresponding rises in 5 other domains which had previously shown no change; suggesting that these are secondary failures.

This indicates that whilst many regions of strain localisation are formed (as clearly evident in Fig. 5), not all of them develop and contribute to the final failure of the sample. It is proposed these regions of strain localisation are due to micro-cracks, and that the failure of the samples is preceded by formation of a critical crack nucleus from the coalescence of micro-cracks.

This process was investigated using an extreme value statistical approach. The maximum strain error within each domain was recorded and arranged in order of magnitude. Since all the individual tests are independent, it was possible to repeat this process and collate the maximum strain errors from each test into a single sorted dataset. It was anticipated that increasing the dataset size in this way would increase the resolution at which the distribution may be characterised.

For a double exponential maximum value distribution (Gumbel distribution) the cumulative distribution function, F_j is given by the following equation:

$$F_j = \frac{j}{n+1}, \tag{2}$$

where n is the total number of values and j is the jth value sorted from smallest to largest. The reduced variate, y_j may then be written as

$$y_j = -\ln[-\ln(F_j)] = -\ln\left[-\ln\left(\frac{j}{n+1}\right)\right]. \tag{3}$$

The results are plotted in Fig. 7, where the reduced variate y_j has been written to reflect the actual cumulative sampled area. The results should appear as a straight line if they may be adequately characterised by a single extreme value distribution (see Fig. 8).

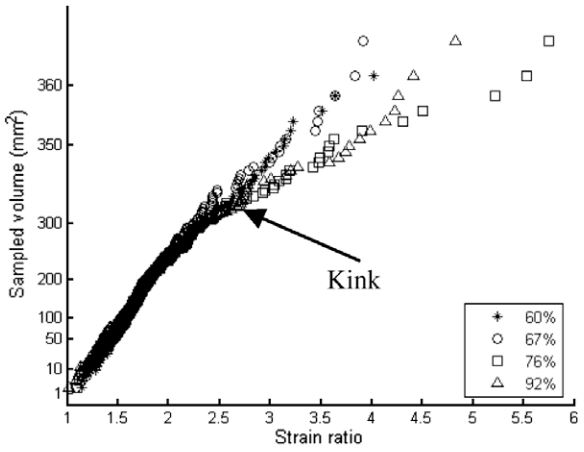

Fig. 8. Extreme value distributions with increasing load.

In the disc compression tests, the distribution of low strain ratios is constant at all load levels. Furthermore, at low loads this distribution appears constant for the full range of strain ratios observed. However, at 76% and 92% of failure load, a marked kink is present above a strain ratio of ~2.5 indicating that all these points do not originate from a common distribution.

7. Discussion

The analysis has shown that apparent global elastic properties may be derived by measuring the surface deformation fields and then correlating these with a finite element solution. The elastic moduli were only obtained at moderate to high strains as the errors inherent within the ESPI technique are at their most significant due to the small strain increments relative to the preloaded state at the beginning of the disc compression test. Direct comparison of the Young's modulus with results with literature values is not possible due to the non-uniform and biaxial stress state in the disc compression sample. However, the average values are as expected, although the highly non-linear stress strain response reported by other authors was not observed.

The observed rise in the derived Poisson's ratio with increasing load appears to be significant, and a possible mechanism may be a gradual onset of diffuse micro-cracking. This has been observed, using X-ray micro-tomography, in strained graphite of the same microstructure [1]. The micro-cracks would be expected to be aligned perpendicular to the maximum tensile stress, reducing the elastic modulus in this direction [8]. The consequent elastic anisotropy would be manifest in the derived Poisson's ratio, since the analysis assumes isotropic behaviour. The observed rise in Poisson's ratio is thus understood to be a consequence of the specimen geometry, and is not the intrinsic material property. The implication is that significant micro-cracking occurs at relatively low applied loads in the disc compression test.

Fitting a finite element solution to the measured data, permitted the removal of the strain fields intrinsic to the sample geometry and hence allowed characterisation of the local perturbations of the in-plane surface displacements due to microstructural inhomogeneities. The general microstructural strain ratio distribution appears to be Gaussian. However, near to the failure load, the high strain tail of the distribution becomes more developed. These regions of very high strain localisation were shown not to be randomly distributed but rather were localised at discrete points. Tracking the evolution of these features showed that the majority behave linearly (i.e. give a constant strain concentration) throughout the test duration with significant non-linear behaviour being restricted to only a small number of features. An extreme value statistics methodology was applied to investigate these outliers. It appears that at low loads that the outlier population may be considered as a single distribution. However, the presence of a distinct kink in Fig. 7 indicates that above applied loads of ~75% failure a second population of features is evident. This suggests that the surface features associated with failure are separable from those causing random microstructural strain perturbations. Further work is on-going to characterise the nature and spatial distribution of these critical microstructural features.

8. Conclusions

Young's modulus and Poisson's ratio may be successfully derived from disc compression samples, by optical strain mapping of the surface strain fields during loading.

The distribution of microstructural strains is generally Gaussian at low loads, with evidence increasing strain localisation at higher loads.

It is proposed that the failure of the samples is preceded by formation of a critical crack nucleus from the coalescence of microcracks.

It is suggested that the critical microstructural features associated with failure exist as a second population, with a significantly lower spatial frequency than the features associated with random microstructural strain localisation.

Acknowledgements

The authors would like to thank British Energy Generation Ltd. for financial and material support under project GRA/GNSR/6022. The opinions expressed in the paper are those of the authors, and not necessarily those of British Energy plc.

References

[1] A. Hodgkins, T.J. Marrow, P. Mummery, B. Marsden, A. Fok, in: Proceedings of Application of X-ray tomography to study fracture and crack growth, Churchill College, Cambridge, 7–8 April 2005.
[2] A. Rudnick, A.R. Hunter, F.C. Holden, Mater. Res. Standards 3 (4) (1963) 283.
[3] H. Awaji, S. Sato, J. Eng. Mater. Tech. 101 (1979) 139.
[4] Q.Z. Wang, X.M. Jia, S.Q. Kou, Z.X. Zhang, P.-A. Linqvist, Int. J. Rock Mech .Ming. Sci. 41 (2004) 245.
[5] K.-M. Hung, C.-C. Ma, J. Exp Mech. 43 (2) (2003) 216.
[6] Z. Wang, J.F. Cardenas-Garcia, B. Han, J. Exp. Mech. 45 (1) (2005) 27.
[7] R. Taylor, R.G. Brown, K. Gilchrist, E. Hall, A.T. Hodds, B.T. Kelly, F. Morris, Carbon 5 (1967) 519.
[8] R. Talreja, S. Yalvac, L.D. Yats, D.G. Wetters, J. Compos. Mater. 26 (1992) 1644.